PHYSICAL REVIEW C **108**, 024304 (2023)

New insights into backbending in the symmetry-adapted shell-model framework

Nicholas D. Heller,[1] Grigor H. Sargsyan,[2,3] Kristina D. Launey,[4] Calvin W. Johnson,[5]
Tomáš Dytrych,[2,5] and Jerry P. Draayer[4]
[1]*Department of Physics, Harvey Mudd College, Claremont, California 91711, USA*
[2]*Department of Physics and Astronomy, Louisiana State University, Baton Rouge, Louisiana 70803, USA*
[3]*Lawrence Livermore National Laboratory, Livermore, California 94550, USA*
[4]*Department of Physics, San Diego State University, San Diego, California 92182, USA*
[5]*Nuclear Physics Institute of the Czech Academy of Sciences, 25068 Řež, Czech Republic*

(Received 17 May 2022; revised 6 June 2023; accepted 20 June 2023; published 8 August 2023)

We provide insights into the backbending phenomenon within the symmetry-adapted framework which naturally describes the intrinsic deformation of atomic nuclei. For ^{20}Ne, the canonical example of backbending in light nuclei, the *ab initio* symmetry-adapted no-core shell model shows that while the energy spectrum replicates the backbending from experimental energies under the rotor-model assumption, there is no change in the intrinsic deformation or intrinsic spin of the yrast band around the backbend. For the traditional example of ^{48}Cr, computed in the valence shell with empirical interactions, we confirm a high-spin nucleus that is effectively near-spherical, in agreement with previous models. However, we find that this spherical distribution results, on average, from an almost equal mixing of deformed prolate shapes with deformed oblate shapes. Microscopic calculations confirm the importance of spin alignment and configuration mixing, but surprisingly unveil no anomalous increase in moment of inertia. This finding opens the path toward further understanding the rotational behavior and moment of inertia of medium-mass nuclei.

DOI: 10.1103/PhysRevC.108.024304

I. INTRODUCTION

Backbending refers to an anomalous increase in nuclear moment of inertia along the yrast band at some critical angular momentum. Based on experimental energy spectra, backbending is found to occur in nuclei ranging from ^{20}Ne through ^{48}Cr to the actinide region. Understanding the backbending phenomenon is essential to resolve the elusive physics of the high angular-momentum rotational behavior of strongly deformed nuclei. Possible explanations of this phenomenon relate to the physics of spin alignment due to Coriolis force pair-breaking [1,2], phase transitions between irrotational and rigid rotor flow, and shape coexistence [3]. Theoretically testing these explanations has been restricted to heavier nuclei, for many of which microscopic A-body descriptions are intractable computationally.

In this paper, we provide an *ab initio* study of the backbending phenomenon for ^{20}Ne, a canonical example of backbending in light nuclei [4], with a focus on translationally invariant moments of inertia and intrinsic deformation and triaxiality. We use *ab initio* wave functions for ^{20}Ne from our earlier study [5] calculated in the symmetry-adapted no-core shell model (SA-NCSM) [5,6]. The SA-NCSM provides nuclear wave functions in terms of SU(3) $\supset$ SO(3) basis states without breaking the rotational symmetry. The SU(3) quantum numbers, in turn, directly provide the intrinsic nuclear deformation in the body-fixed frame [6]. We show that the energy spectrum of ^{20}Ne replicates the backbending from experimental energies under the rotor-model assumption, but interestingly, the *ab initio* results show no change in the intrinsic deformation or intrinsic spin of the yrast band around the backbend in ^{20}Ne. To further understand this, we examine spin alignment in low-lying states in ^{20}Ne.

For the last two decades, the heavier nucleus of ^{48}Cr has been a key example of backbending, because it tests the predictions of both mean-field and configuration-interaction methods. Almost all previous studies of ^{48}Cr find an yrast band with an intrinsic prolate deformation before the backbend, and, after the backbend, find that ^{48}Cr transitions towards sphericity and with a lack of an intrinsic state above the backbend (see for example [7–16], and Ref. [17] for a detailed model comparison). However, when Herrera *et al.* [17] decomposed configuration-interaction shell-model wave functions into components specified by the eigenvalues of the SU(3) second-order Casimir invariant operator, they found consistently large deformations above the backbend rather than sphericity. While the full SU(3) content of the wave function provides information about the intrinsic deformation and rotational bands [5,18–23], the second-order Casimir invariant alone is not sufficient to fully decompose into SU(3) irreducible representations (irreps) and distinguish between prolate, oblate, and triaxial deformations.

To resolve this apparent contradiction about the structure of ^{48}Cr after the backbend, we again employ the symmetry-adapted framework. To understand the results of Ref. [17], we utilize the same model conditions as those used in [17] for ^{48}Cr, namely, a core of inactive particles, valence-shell model space, and an empirical interaction for the pf shell. With this, we can now compute ^{48}Cr wave functions in a

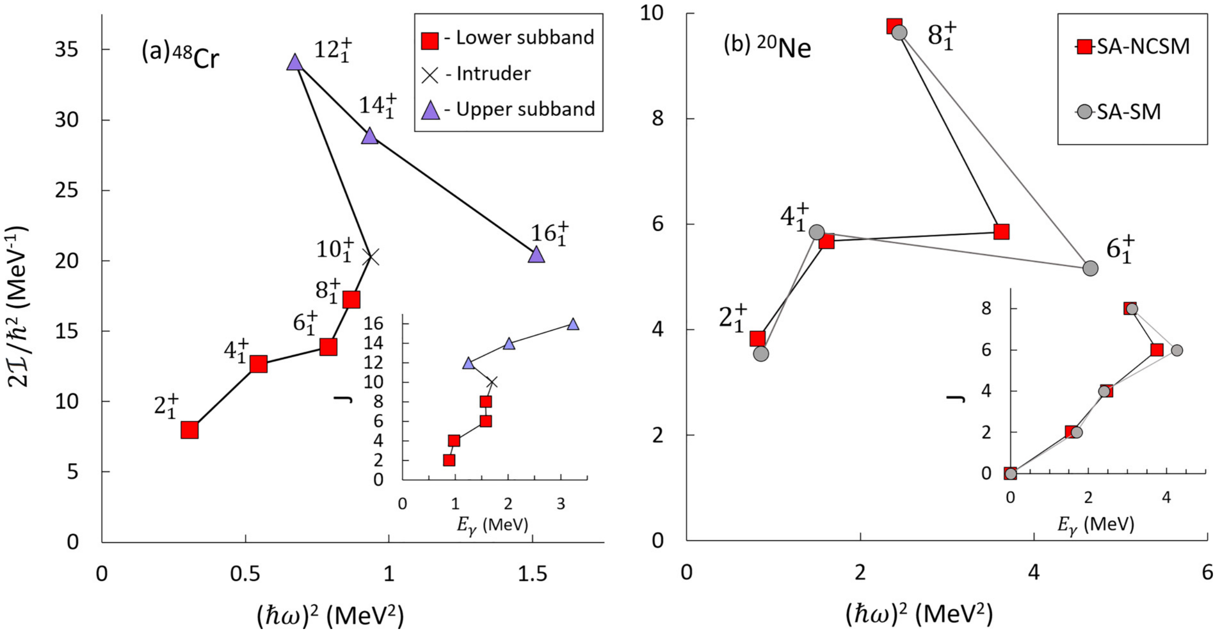

FIG. 1. Backbending of ^{48}Cr at $J = 12$ and of ^{20}Ne at $J = 8$ traditionally seen in $2\mathcal{I}/\hbar^2$ vs $(\hbar\omega)^2$ [3] as well as J vs. E_γ (insets), based on Eq. (2) and excitation energies calculated for: (a) ^{48}Cr in the SA-SM with the GXPF1 interaction, and (b) for ^{20}Ne in the SA-NCSM with the NNLO$_{\text{opt}}$ chiral potential for $\hbar\Omega = 15$ MeV and $N_{\max} = 8$ (blue squares), and in the SA-SM with the USDA interaction (gray circles). Excitation energies are in close agreement with experiment, as shown in Fig. 2.

configuration-interaction framework with complete information about intrinsic deformation. We show that for the yrast band above the backbend the deformed configurations observed in Ref. [17] are a part of a remarkably balanced mixing of prolate and oblate intrinsic shapes, which leads to a nucleus that appears near spherical on average. This reconciles the outcomes of Ref. [17] and previous studies.

Similarly to ^{20}Ne, our results for ^{48}Cr do not show an anomalous change in moment of inertia at the backbend, suggesting that a rigid shape change is not the sole mechanism for the backbend.

The outcomes of our study for ^{20}Ne and ^{48}Cr emphasize the importance of band crossing and spin-alignment in driving backbending, which affects the energy of the states, but with only very little effect on the nuclear spatial distribution.

II. THEORETICAL FRAMEWORK

A. Backbending and the rotor model: A traditional approach

Backbending is, in principle, observed from applying the rotor model to high-spin energy spectra. The rigid rotor Hamiltonian is

$$\hat{H} = \text{const} + \frac{\hbar^2}{2\mathcal{I}}\hat{J}^2 \tag{1}$$

with eigenvalues $E(J) = E_0 + \frac{\hbar^2}{2\mathcal{I}}J(J+1)$, where $\mathcal{I}$ is the moment of inertia and $\hat{J}$ is the total angular momentum operator.[1] Traditionally, the anomalous increase in the moment of inertia has been identified from the dependence of $2\mathcal{I}/\hbar^2$ on the nuclear rotational frequency $(\hbar\omega)^2$ derived from the rotor-model excitation energies [1] (e.g., see Fig. 1):

$$\frac{2\mathcal{I}}{\hbar^2} = \frac{4J-2}{E_\gamma} \quad (\hbar\omega)^2 = (J^2 - J + 1)\left(\frac{E_\gamma}{2J-1}\right)^2, \tag{2}$$

where $E_\gamma = E(J) - E(J-2)$ is the excitation energy. In Eq. (2), $\mathcal{I}$ is derived from the first discrete derivative of $E(J)$ with respect to $J(J+1)$, whereas $\hbar\omega$ is derived from the rotational energy at midpoint $\frac{E(J)+E(J-2)}{2} \sim \frac{1}{2}\frac{\mathcal{I}}{\hbar^2}(\hbar\omega)^2$ (e.g., see [25]).

B. Symmetry-adapted framework

Ab initio descriptions of spherical and deformed nuclei up through the calcium region are now possible with the *ab initio* SA-NCSM without the use of interaction renormalization procedures, as reviewed in Refs. [6,18]. In particular, we have shown that the SA-NCSM, using the SU(3)-adapted basis [18] or the Sp(3, ℝ)-adapted basis [5,26], can use significantly reduced model spaces as compared to the corresponding ultralarge conventional model spaces without compromising the accuracy of results for various observables. This allows the SA-NCSM to accommodate larger model spaces and to reach heavier nuclei, such as ^{20}Ne [5], ^{21}Mg [27], ^{22}Mg [28], ^{28}Mg [29], as well as ^{32}Ne and ^{48}Ti [6].

The SA-NCSM with SU(3)-adapted basis solves the many-body nuclear Hamiltonian in basis states that are labeled

---

[1] In general, $\hat{H} = \text{const} + \sum_j \frac{\hbar^2}{2\mathcal{I}_j}\hat{J}_j^2$, where $\mathcal{I}_j$ are the moments of inertia relative to a set of body-fixed (principal) axes, $j = 1, 2$, and 3.

Yrast states can be effectively described by an intrinsic deformation rotating perpendicular to the three-axis with $\mathcal{I} \sim \mathcal{I}_1 \sim \mathcal{I}_2$ [24].

schematically as

$$|\vec{\gamma}; N(\lambda\,\mu)\kappa L; (S_p S_n)S; JM\rangle, \tag{3}$$

where S_p, S_n, and S denote proton, neutron, and total intrinsic spins, respectively, N is the total number of harmonic oscillator (HO) excitation quanta, and $(\lambda\,\mu)$ represent a set of quantum numbers that labels an SU(3) irrep. The label κ distinguishes multiple occurrences of the same orbital angular momentum L in the parent irrep $(\lambda\,\mu)$. The L is coupled with S to the total angular momentum J and its projection M. The symbol $\vec{\gamma}$ schematically denotes the additional quantum numbers needed to specify a distribution of nucleons over the major HO shells and their single-shell and intershell SU(3) quantum numbers. All of these labels uniquely determine the SA-NCSM basis states (3) [18]. Note that in this paper, we use N given by the total HO energy $N\hbar\Omega$ of all particles (for a HO frequency $\hbar\Omega$), and for example, $N = 50$ ($N = 156$) for the valence-shell configurations of ^{20}Ne (^{48}Cr).

For comparatively large model spaces, it is often advantageous to assume a core of inactive particles. For this, we introduce a core in the SA-NCSM and allow only the valence particles to excite to higher shells. This approximate model is henceforth referred to as the symmetry-adapted shell model (SA-SM). When solved only in the valence shell with empirical interactions, it coincides with earlier valence-shell models with SU(3) $\supset$ SO(3) basis [30–41]. For the SA-SM, we transform the effective one-body interactions (Appendix A) and two-body matrix elements [42] to the SU(3) basis. In this study, we apply the valence-shell SA-SM with empirical interactions to ^{48}Cr with a ^{40}Ca core, and to ^{20}Ne with a ^{16}O core. For ^{20}Ne, we also employ the *ab initio* SA-NCSM for comparison.

Following Ref. [19], we identify rotational bands as states that exhibit quasidynamical SU(3) symmetry. Namely, the corresponding wave functions have similar $(\lambda\,\mu)$ decomposition. Alternatively, the wave function can be expressed in terms of the C_2 eigenvalues of the second-order SU(3) Casimir invariant, as done in Ref. [17], where

$$C_2(\lambda,\mu) = \tfrac{2}{3}(\lambda^2 + \mu^2 + \lambda\mu + 3\lambda + 3\mu). \tag{4}$$

Since C_2 eigenvalues are symmetric under the exchange of λ and μ, we will need a second measure to determine if a deformation is prolate ($\lambda > \mu$), triaxial ($\lambda = \mu$), or oblate ($\lambda < \mu$), as discussed in the next section. In this study, we also use the C_3 eigenvalues of the third-order SU(3) Casimir invariant operator, proportional to $\lambda - \mu$, which provide exactly this (see, e.g., [43])

$$C_3(\lambda,\mu) = \tfrac{1}{9}(\lambda - \mu)(\lambda + 2\mu + 3)(2\lambda + \mu + 3) \tag{5}$$

with $C_3 > 0$ ($C_3 < 0$) for prolate (oblate) and $C_3 = 0$ triaxial.

C. Intrinsic deformation and moments of inertia

The SU(3) basis is ideal for calculations of the *microscopic intrinsic* moments of inertia. The moments of inertia operators are defined as

$$\hat{\mathcal{I}}_z = \sum_{i=1}^{A} m\left(r_i^2 - z_i^2\right), \hat{\mathcal{I}}_x = \sum_{i=1}^{A} m\left(r_i^2 - x_i^2\right), \hat{\mathcal{I}}_y = \sum_{i=1}^{A} m\left(r_i^2 - y_i^2\right), \tag{6}$$

where m is the nucleon mass, A is the total number of particles, and $\mathbf{r}_i$ is the coordinate of the ith particle relative to the center of mass with projection z_i along the z direction, the axis of quantization.

For each basis state (3), the SU(3) quantum numbers $N(\lambda\,\mu)$ fully define an extremal-weight (EW) state $|\phi_0^{N(\lambda\,\mu)}\rangle$ (or simply $|\phi_0\rangle$), similarly to $|\phi_0^J\rangle = |J, M = J\rangle$ that is the highest-weight SU(2) state, from which all other $|JM\rangle$ states can be induced through the lowering $\hat{J}_-$ operator; equivalently all states can be induced through the raising $\hat{J}_+$ operator on the lowest-weight SU(2) state $|J, M = -J\rangle$. As discussed below, this extremal-weight SU(3) state has been shown to practically coincide with an *intrinsic* state [44], defined as an eigenstate of the quadrupole moment operator.

The expectation value of the moment of inertia (6) for the extremal-weight state $|\phi_0\rangle$ can be readily calculated using (see, e.g., [45]) $\langle\phi_0|\sum_i z_i^2|\phi_0\rangle = b^2(N_z - \frac{1}{2})$, $\langle\phi_0|\sum_i x_i^2|\phi_0\rangle = b^2(N_x - \frac{1}{2})$, and $\langle\phi_0|\sum_i y_i^2|\phi_0\rangle = b^2(N_y - \frac{1}{2})$, where subtracting 1/2 ensures the removal of the center-of-mass spurious contribution (see Appendix C), and where $b = \sqrt{\hbar/m\Omega}$ is the HO length and N_x, N_y, and N_z are HO quanta along the three directions with $N = N_x + N_y + N_z$. For $N_z \geqslant N_x \geqslant N_y$, $\lambda = N_z - N_x$ and $\mu = N_x - N_y$, and hence, $|\phi_0\rangle$ can be equally specified as $|\phi_0^{N_z N_x N_y}\rangle$. For the extremal-weight state $|\phi_0\rangle$, our codes use the convention of the lowest-weight state $|\phi_{LW'}\rangle$ for $\lambda \geqslant \mu$ and the highest-weight states $|\phi_{HW'}\rangle$ for $\lambda < \mu$, as detailed in [46,47]. For a complete labeling of SU(3) states $|N(\lambda\,\mu)\epsilon\Lambda M_\Lambda\rangle$ according to the SU(3) $\supset$SU(2) canonical group chain, all the additional labels of $|\phi_0\rangle$ are specified through λ and μ only [46]:

$$\begin{aligned} \lambda \geqslant \mu\,(LW') &: \epsilon = 2\lambda + \mu,\ \Lambda = M_\Lambda = \frac{\mu}{2}, \\ \lambda < \mu\,(HW') &: \epsilon = -(\lambda + 2\mu),\ \Lambda = -M_\Lambda = \frac{\lambda}{2}. \end{aligned} \tag{7}$$

Most importantly, the matrix elements of the monopole operator $\sum_i r_i^2$ and the quadrupole moment $\hat{Q}_{2m} = \sum_i \sqrt{16\pi/5}\, r_i^2 Y_{2m}(\hat{\mathbf{r}}_i)$ with, e.g., $\hat{Q}_{20} = \sum_i (3z_i^2 - r^2)$, are expressed only in terms of N, λ, and μ for the extremal-weight state:

$$\begin{aligned} \langle\phi_0|\sum_i r_i^2\,|\phi_0\rangle &= b^2\left(N - \frac{3}{2}\right), \\ \langle\phi_0|\hat{Q}_{20}|\phi_0\rangle &= b^2\epsilon \equiv q_0, \\ \langle\phi_0|\hat{Q}_{2\pm1}|\phi_0\rangle &= 0, \\ \langle\phi_0|\hat{Q}_{2\pm2}|\phi_0\rangle &= b^2\sqrt{\frac{3}{2}}2M_\Lambda \equiv q_2 \end{aligned} \tag{8}$$

(cf. [45]). In the rotor limit of SU(3) (for large λ and μ), $|\phi_0\rangle$ is indeed an eigenstate of $\hat{Q}_{2m}$, $\hat{Q}_{2m}\,|\phi_0\rangle = q_m\,|\phi_0\rangle$ (cf. Eq. (6) of Ref. [48]).[2] Hence, in this limit, the SU(3) extremal-weight state corresponds to an intrinsic rotor state with intrinsic quadrupole moments given by $q_{0,2}$ [49]. For this state, we can then define the body-fixed frame with principal axes 1, 2, and 3, such that $q_0 = 2Q_3 - Q_1 - Q_2 = b^2\epsilon$ and $q_2 = \sqrt{\frac{3}{2}}(Q_1 - Q_2) = \sqrt{6}b^2M_\Lambda$. Using that $\sum_j Q_j = 0$, the intrinsic quadrupole moments along the one-, two-, and three-axis are given in this limit as

$$\frac{Q_3}{b^2} = \frac{\epsilon}{3}, \frac{Q_1}{b^2} = -\frac{\epsilon}{6} + M_\Lambda, \frac{Q_2}{b^2} = -\frac{\epsilon}{6} - M_\Lambda. \tag{9}$$

These are expressed through λ and μ using Eq. (7). This relation is important, since it directly relates λ and μ to the intrinsic deformation of each SU(3) basis state (3). We note that this relation is exact in the limit and practically holds for most SU(3) basis state, whereas it is a very good approximation even when λ and μ are both small (typically, it is sufficient to ensure that $L < |\epsilon|$ [48] for a given λ and μ, which is usually the case since the maximum possible L is $L_{\max} = \lambda + \mu < |\epsilon|$).

We note that the descriptions in terms of the highest and lowest-weight states are equivalent, they only differ by the choice of the principal axes. For the choice of Eq. (7), the intrinsic state will have a prolate shape for $\lambda > \mu$ with positive intrinsic quadrupole moment $Q_3 = q_0/3$ along the axis of symmetry (three-axis) that coincides with the z quantization axis (with $\lambda = \mu$ being triaxial); for $\lambda < \mu$, the intrinsic state will be oblate with negative intrinsic quadrupole moment q_0 along the three-axis that also coincides with the z quantization axis. This choice is therefore very convenient in considering their rotor limit (cf. Ref. [48]).

For nuclear wave functions $|J^\pi\rangle$ in the SU(3) basis (3) with probability amplitudes $(c^J_{N(\lambda\,\mu)})^2$, one can calculate the intrinsic quadrupole moment as (cf. Eq. (25) of Ref. [48])

$$q_0^J = \sum_{N(\lambda\,\mu)} \left(c^J_{N(\lambda\,\mu)}\right)^2 q_0(\lambda, \mu), \tag{10}$$

where $q_0(\lambda, \mu)$ is defined in Eq. (8) as q_0 for given λ and μ. This, as discussed in Ref. [48], effectively describes a soft-rotor rotational band consisting of rotational states that share a common intrinsic state, which is an admixture of eigenstates of the quadrupole moment. While the quadrupole moment observable $Q(J) = \langle J^\pi|\hat{Q}_{20}|J^\pi\rangle$ is calculated exactly in the SA-NCSM using the physically relevant basis (3) with complete labeling $|N(\lambda\,\mu)\kappa LM\rangle$ according to the SU(3) $\supset$ SO(3) group chain, the convention (7) allows one to directly use the rotor-model estimate[3]

$$Q(J, K=0) \approx C^{JJ}_{JJ,20}C^{J0}_{J0,20} \sum_{N(\lambda\,\mu)} \left(c^J_{N(\lambda\,\mu)}\right)^2 q_0(\lambda, \mu). \tag{12}$$

Note that the approximations arise when we aim to compare to the rotor-model estimate, while exact expressions are obtained when using the SA-NCSM code. for a given K band, $Q_{\text{rot}}(J, K) = C^{JJ}_{JJ,20}C^{JK}_{JK,20}q_0^J$ (see, e.g., [24]) with q_0^J given by Eq. (10).

Finally, the intrinsic (body-fixed) moments of inertia can be calculated using Eq. (8) and their relation to the intrinsic matter quadrupole moments $2\frac{\mathcal{I}_j}{m} = \frac{4}{3}(r^2 - \frac{3}{2}Q_j)$, for $j = 1, 2$ and 3:

$$\begin{aligned}
\frac{2}{\hbar^2}\langle\phi_0|\mathcal{I}_3|\phi_0\rangle &= \frac{4}{3\hbar\Omega}\left(N - \frac{3}{2} - \frac{\epsilon}{2}\right),\\
\frac{2}{\hbar^2}\langle\phi_0|\mathcal{I}_1|\phi_0\rangle &= \frac{4}{3\hbar\Omega}\left(N - \frac{3}{2} + \frac{\epsilon}{4} - \frac{3}{2}M_\Lambda\right),\\
\frac{2}{\hbar^2}\langle\phi_0|\mathcal{I}_2|\phi_0\rangle &= \frac{4}{3\hbar\Omega}\left(N - \frac{3}{2} + \frac{\epsilon}{4} + \frac{3}{2}M_\Lambda\right).
\end{aligned} \tag{13}$$

This yields the translationally invariant and body-fixed moments of inertia for each basis state (3), which can be expressed in terms of N, λ, and μ only. We note that $\mathcal{I}_3$ can be generalized beyond the valence shell to multishells, as discussed in Appendix B.

We use Eq. (13) with our code convention (7) to calculate the moment of inertia for each SU(3) basis state, and take the probability-weighted sum to find the microscopic moment of inertia of the entire wave function (C6). While SU(3) basis states are regarded as rigid rotors, nonrigid degrees of freedom such as spin-coupling or phase transitions manifest themselves through the SU(3) mixing that results from the nuclear interaction.

D. Mapping to shape parameters β and γ

The connection to an intrinsic state in the SU(3) scheme establishes a mapping of the quantum numbers $(\lambda\;\mu)$ of the SU(3) basis states (3) to the collective shape parameters, namely, the deformation β and triaxiality γ [44,49]. In general, the β and γ parameters are defined through the intrinsic quadrupole moments $\bar{q}_0$ and $\bar{q}_2$, $k_0\beta\cos\gamma = \bar{q}_0$, and $\frac{1}{\sqrt{2}}k_0\beta\sin\gamma = \bar{q}_2$ for a suitable normalization constant k_0.

---

[2] In a single valence shell, $\hat{Q}_2 = \sqrt{3}\hat{C}_2^{(1\,1)}$, where $C_2^{(1\,1)}$ is an SU(3) generator that does no mix $(\lambda\,\mu)$ configurations, $|\phi_0\rangle$ is an eigenstate of $\hat{Q}_{20}$ for any λ and μ.

[3] As an illustrative example, one can show that for a $K = 0$ band ($\kappa \approx 0$) for a valence shell

$$\begin{aligned}
&(\lambda\,\mu)\kappa L'MQ_{20}(\lambda\,\mu)\kappa LM\\
&\quad = C^{L'M}_{LM,20}\frac{\langle(\lambda\,\mu)\kappa L;(1\,1)02\|(\lambda\,\mu)\kappa L'\rangle}{\langle(\lambda\,\mu)\epsilon\Lambda;(1\,1)00\|(\lambda\,\mu)\epsilon\Lambda\rangle_{EW}}q_0(\lambda, \mu)\\
&\quad \approx C^{L'M}_{LM,20}C^{L'0}_{L0,20}\sqrt{\frac{2L+1}{2L'+1}}q_0(\lambda, \mu)
\end{aligned} \tag{11}$$

(the approximation is about 5–20 % and verified with the SU(3) package [47]; the largest approximations arise for λ and μ that are small and comparable to L). This, for low spin and high J, yields the rotor expression for the quadrupole moment.

These can be calculated from the expectation values of two scalars in the laboratory frame, $\frac{1}{2}\mathrm{tr}Q^2 = \frac{1}{12}\langle Q\cdot Q\rangle = \frac{1}{12}k_0^2\beta^2$ and $\frac{1}{3}\mathrm{tr}Q^3 = -\frac{1}{108}\sqrt{\frac{7}{2}}\langle [Q\times Q]_2\cdot Q\rangle = \frac{1}{108}k_0^3\beta^3\cos 3\gamma$, with k_0 determined from the liquid drop model as $k_0/3b^2 \equiv k = \sqrt{5/9\pi}Ar_{\mathrm{rms}}^2/b^2$ for a root-mean-square (rms) radius $r_{\mathrm{rms}} = \sqrt{\langle r^2\rangle/A}$ (cf. Ref. [43] for k and Ref. [50] for k_0). As mentioned above, in the rotor limit (large λ and μ), the SU(3) extremal-weight state becomes an eigenstate of Q, thereby q_0 and q_2 of Eq. (8) coincide with $\bar{q}_0$ and $\bar{q}_2$, respectively. Hence (using k),

$$k\beta\cos\gamma = \frac{\epsilon}{3},\ k\beta\sin\gamma = \frac{1}{\sqrt{3}}2M_\Lambda,\ \text{with}\ \tan\gamma = \frac{\sqrt{12}M_\Lambda}{\epsilon}. \tag{14}$$

This relation maps each SU(3) basis state with $(\lambda\,\mu)$ to an average ellipsoid with deformation β and triaxiality γ [43,51]. Equation (14) provides the exact relation for q_0 for valence-shell calculations with

$$k = \sqrt{\frac{5}{9\pi}}\left\langle\sum_i \frac{r_i^2}{b^2}\right\rangle = \sqrt{\frac{5}{9\pi}}\left(N-\frac{3}{2}\right) \tag{15}$$

(see, e.g., [52]). For the rotor-like choice of Eq. (7), this implies that $k\beta\cos\gamma$ and $k\beta\sin\gamma$ are both positive for prolate shapes and both negative for oblate shapes, whereas $\tan\gamma \geqslant 0$. With β being the magnitude of deformation, this implies that $0^\circ \leqslant \gamma \leqslant 30^\circ$ for $\lambda \geqslant \mu$ and $180^\circ \leqslant \gamma < 210^\circ$ for $\lambda < \mu$. However, a natural choice is β to adopt the sign of ϵ and reflect the displacement along the three-axis from the nondeformed spherical shape, implying $0^\circ \leqslant \gamma \leqslant 30^\circ$ with $\beta > 0\,(< 0)$ for prolate (oblate) shapes. Importantly, this naturally links to mean-field frameworks, especially when triaxiality is neglected ($\gamma = 0^\circ$ with $k_0\beta = q_0$).

Similarly, as derived in Ref. [53,54] for a valence shell and $L^2 < 2C_2$, for each SU(3) basis state β and γ can be determined through the SU(3) Casimir invariants of Eqs. (4) and (5):

$$\begin{aligned}\frac{3}{2}k^2\beta^2 &= C_2(\lambda,\mu),\\ \frac{3}{4}k^3\beta^3\cos 3\gamma &= C_3(\lambda,\mu) \sim (\lambda-\mu)\end{aligned} \tag{16}$$

with k defined in Eq. (15). While the Casimir invariants provide a unique solution for $k^2\beta^2$ and $k\beta\cos 3\gamma$, in general, there are multiple solutions for β and γ: $k\beta = \pm\sqrt{\frac{2}{3}C_2(\lambda,\mu)}$ and $\cos 3\gamma = \pm\frac{\sqrt{6}C_3(\lambda,\mu)}{C_2(\lambda,\mu)^{1/3}}$. Indeed, for oblate shapes $[C_3(\lambda,\mu) < 0]$, using $\beta < 0$ and $0^\circ \leqslant \gamma < 30^\circ$ corresponds to Eq. (14) and the associated rotor limit with the three-axis and z axis aligned (cf. Ref. [48], Sec. 3.3). We note that Eq. (16) maps a nuclear state to an average ellipsoid with β and γ only when the state consists of a single SU(3) configuration. In the case of mixing of SU(3) configurations, in general, the state can no longer be viewed as a single ellipsoid for which β and γ are determined through the $\langle C_2\rangle$ and $\langle C_3\rangle$ expectation values. The state is instead a liner superposition of rigid ellipsoids, each of which has β and γ determined from Eq. (16), or equivalently from Eq. (14), as discussed next.

For completeness, we mention other mappings $(\beta,\gamma) \leftrightarrow (\lambda,\mu)$ available in the literature. For $C_2 \gg 2$, which is practically the case for most SU(3) states, Ref. [54] uses Eq. (16) to obtain $k\beta\cos\gamma = (2\lambda+\mu+3)/3$ and $k\beta\sin\gamma = (\mu+1)/\sqrt{3}$ for prolate shapes. Reference [48] provides a multishell generalization based on the rotor expansion of SU(3) $\subset$ Sp(3, $\mathbb{R}$), namely, for prolate shapes in a K band: $k\beta\cos\gamma = (2\lambda+\mu+3)/3$ and $k\beta\sin\gamma = \sqrt{(\mu-K)(\mu+K+2)/3}$, and for oblate shapes: $k\beta\cos\gamma = -(\lambda+2\mu+3)/3$ and $k\beta\sin\gamma = -\sqrt{(\lambda-K)(\lambda+K+2)/3}$, valid for small L and large λ or μ. Notably, these relations for $\beta\cos\gamma$ and $\beta\sin\gamma$ (for low K) agree with each other and coincide with Eq. (14) used in this paper at $\mathcal{O}(1/N)$.

III. RESULTS

We explore the backbending phenomenon by calculating moments of inertia for the yrast band of ^{20}Ne and ^{48}Cr, and by examining the symmetry-adapted wave functions in terms of their expansion in SU(3) basis states.

SA-SM calculations for ^{48}Cr use the pf valence shell, a closed ^{40}Ca core, and the GXPF1 empirical interaction [55] in SU(3) basis, along with an optimal $\hbar\Omega = 10$ MeV. SA-SM calculations for ^{20}Ne use the sd valence shell, a closed ^{16}O core, and the USDA empirical interaction [56] in SU(3) basis. For ^{20}Ne, we compare to the *ab initio* SA-NCSM calculations in 11 HO shells ($N_{\max} = 8$) of Ref. [5] with the NNLO$_{\mathrm{opt}}$ chiral potential [57] for $\hbar\Omega = 15$ MeV (see Figs. 1 and 3 of Ref. [5] for wave functions and energies, respectively). Using these SA-NCSM calculations, we present the first investigation of backbending and moments of inertia for ^{20}Ne within an *ab initio* framework.

A. Moments of inertia: Microscopic vs. energy-spectrum informed

We start with the traditional approach to calculating the moment of inertia as a function of the nuclear rotational frequency $(\hbar\omega)^2$ by using the rotor-model Eq. (2) deduced from excitation energies. Indeed, the SA-SM and SA-NCSM calculations yield energies that reproduce the well-known backbends of ^{48}Cr and ^{20}Ne (Fig. 1).

Likewise, according to Eq. (1), moments of inertia can be extracted within a rotational band if the energy of its states follow the rigid rotor $J(J+1)$ dependence, as shown in Fig. 2 (cf. Ref. [17] for ^{48}Cr). In the SA framework, we organize states into rotational bands according to the dominant SU(3) basis states [18]. To guide the eye, a linear regression for each of the rotational bands identified in Fig. 2 provides a slope that is inversely proportional to the average moment of inertia. In addition, we report the experimental energies of the yrast band, which are in close agreement with the calculations.

Specifically, calculated excitation energies for ^{48}Cr replicate the well-known crossing of two rotational bands: the lower band that starts at the ground state, and the upper band that exhibits strong rigid rotor behavior with a shallower slope, suggesting doubling of the moment of inertia [Fig. 2(a)]. The upper band first appears as an excited state at $J = 8$, and becomes the yrast band at $J = 10$. This crossing

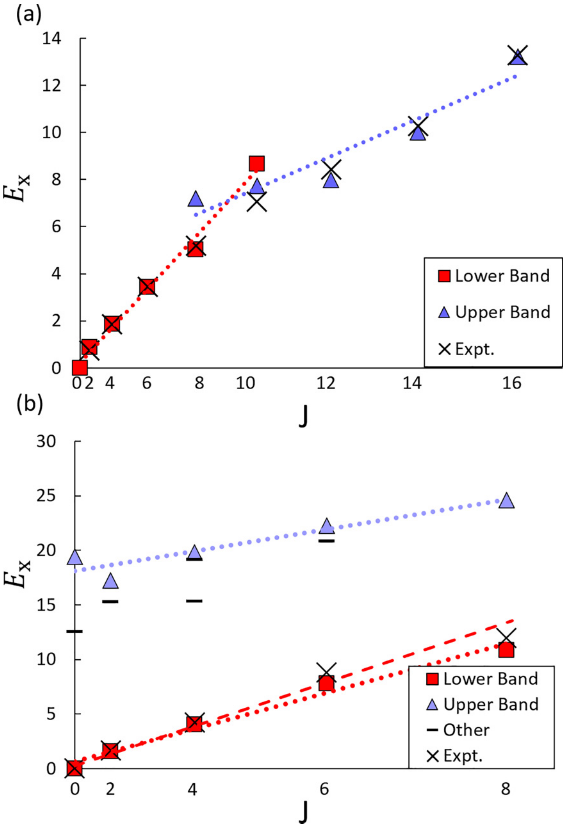

FIG. 2. Excitation energy E_X vs angular momentum J [scaled by $J(J+1)$ to illuminate rotational bands] for (a) ^{48}Cr calculated with the SA-SM with the GXPF1 interaction, and (b) ^{20}Ne calculated with the SA-NCSM with the NNLO$_{\text{opt}}$ chiral potential for $\hbar\Omega = 15$ MeV in $N_{\max} = 8$. The yrast energies are compared to experiment. States are organized in bands according to the dominant SU(3) basis states. Linear regression (dotted line) for each band shows an effective rigid rotor behavior; the linear regression for the lowest four states in ^{20}Ne is also shown (dashed line).

marks the backbend of ^{48}Cr as seen in the dramatic shift in moment of inertia [Fig. 1(a)]. Similarly for ^{20}Ne [Fig. 2(b)], the yrast band displays strong rigid rotor behavior from $J = 0$ to $J = 6$. We note that in Fig. 2(b), the linear regression of the first four states only (dashed line) has a steeper slope than the one up to $J = 8$ (dotted line). Hence, the energy of the lowest 8^+ state is lower compared to the rigid rotor prediction, producing an apparent backbend.

Remarkably, microscopic calculations of the moment of inertia show no anomalous increase for both nuclei (Fig. 3). We calculate microscopic moments of inertia using Eqs. (6) and (C6) by taking into account the position of each particle and with a proper treatment of the center of mass. Microscopic moments of inertia of the yrast band have a magnitude similar to the ones deduced from the experimental energy spectra near and below the backbend, but remain practically unchanged after the backbend. This is also confirmed by the *ab initio* wave functions in ^{20}Ne ($2\mathcal{I}_z/\hbar^2 \approx 3.6$ MeV^{-1}) that do not predict large moment of inertia for 8^+_1 in contrast to the rotor-model results. We note that the SA-SM results suggest an increase in $2\mathcal{I}_z/\hbar^2$, which however is only 4% for the upper band compared to the lower band in ^{48}Cr, and the SA-NCSM calculates only 6% for $J = 8$ in ^{20}Ne (see the inset of Fig. 3). The outcome of Fig. 3 suggests that the microscopic spatial distribution remains practically the same across the states, while the use of the energy spectrum under the rotor-model assumption is likely insufficient to describe moments of inertia, especially since energies can be affected by many other factors (e.g., level repulsion, mixing, spin degrees of freedom, etc.). To explain these findings, we next examine the intrinsic structure of the yrast states in ^{20}Ne and ^{48}Cr.

B. Intrinsic deformation and spin of nuclear states

The symmetry-adapted basis naturally provides decomposition into $(\lambda\ \mu)$ configurations that inform about the intrinsic deformation. From $(\lambda\ \mu)$ we can calculate C_2 eigenvalues Eq. (4) as well as C_3 Eq. (5), along with the shape parameters, β and γ (14). For ^{48}Cr, this expands the C_2 analysis of Ref. [17] and allows us to gain insight into the type of deformation, namely, prolate, oblate or triaxial. Furthermore, we discuss features important to understand the backbending phenomenon by examining ^{20}Ne *ab initio* wave functions.

1. Intrinsic structure of ^{48}Cr

Based on the SU(3) content, we group states in ^{48}Cr into two rotational bands. Confirming the results of Ref. [17], the ground state band appears as the yrast band of ^{48}Cr from $J = 0$ to $J = 8$ and continues through $J = 12$ [Fig. 4(a)]. Here, we show that the GXPF1 renders this band as strongly prolate (see the filled red bars at large C_2 values in Fig. 4a). We recall that large C_2 values correspond to large deformation $\sqrt{C_2} \sim \beta$ according to Eq. (4). At $J \gtrsim 10$ near the "backbend", we find an increased mixing of oblate and triaxial deformations, likely due to the crossing of the upper rotational band (upper sub-band).

Although the upper sub-band still contains large deformations as seen in the C_2 decomposition in Fig. 4, many of these are oblate with C_2 values equal to dominant prolate deformations but with opposite C_3 values (see Fig. 5 for the difference between the lower and upper sub-bands at $J = 8$). Without knowing C_3, the upper band would have been associated with a still overall deformed shape, as suggested in Ref. [17]. The C_3 decomposition can explain this unexpected result, namely, that the yrast band makes a rapid transition at the "backbend" to a strong mixing of prolate and oblate deformations, which on average appears near spherical, but without intrinsic sphericity.

To quantify these results, we use that the intrinsic state is a distribution of intrinsic quadrupole shapes [48], as discussed above, and for each shape, we calculate β according to Eq. (14) and our convention Eq. (7), namely, with positive β for prolate and triaxial ($\lambda \geqslant \mu$), and negative β for oblate deformation ($\lambda < \mu$). An estimate for the overall deformation can be thus provided by an average β_{avg} across all the shapes given their probability amplitudes $c^J_{N(\lambda\mu)}$. The lower sub-band is found to have practically the same β_{avg} for all its states, namely, $\beta_{\text{avg}} \sim 0.12$ and a very large $\langle C_3\rangle \sim 550$–690. For each of these states, the largest deformation is $\beta \sim 0.2$, which is expected to double to $\beta \sim 0.4$ in a complete model

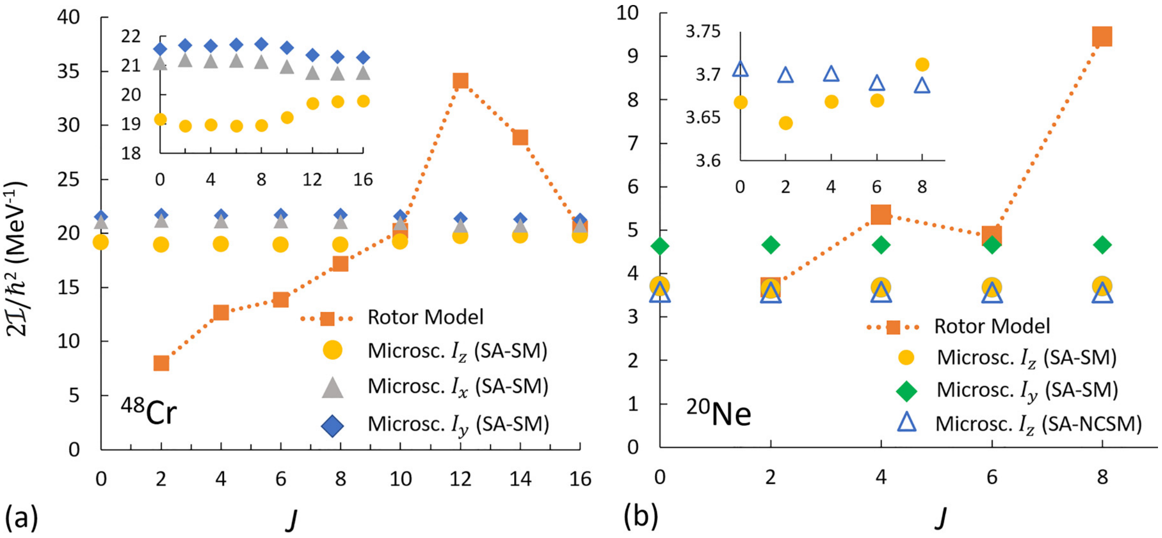

FIG. 3. Moment of inertia $2\mathcal{I}/\hbar^2$ vs angular momentum J for the yrast bands of (a) ^{48}Cr and (b) ^{20}Ne ($I_x \sim I_y$ for SA-SM and hence, not shown). Microscopic moments of inertia use Eq. (13) and are calculated in the SA-(NC)SM framework using Eq. (C6) ("SA-SM" and "SA-NCSM"), whereas the rotor-model moments of inertia use Eq. (2) and experimental energies. Insets: the same without the rotor-model deduced values, showing the slight variations in moments of inertia.

space (see Refs. [48,58] and their discussion on the effect of multishell coupling). Note that, e.g., for 0_1^+, the single (16 4) configuration with the largest C_2 is the most dominant and its contribution is expected to increase in larger model spaces, while the peak in Fig. 4(a) (see 0_1^+) occurs at comparatively smaller C_2 and corresponds to 65 different (14 2) configurations of various spin values. The dominant configurations in the lower sub-band correspond to largely prolate intrinsic deformation, as also observed in Fig. 5(b) for 8_1^+. This prominent prolate structure is in a close agreement with the results reported, e.g., in Refs. [59,60] for the ground state, up to effective charges (and similarly for ^{20}Ne discussed below). Whereas for the upper sub-band, we find relatively smaller values for $\beta_{\rm avg} \sim 0.07$ and $\langle C_3\rangle \sim 100$–170 (see Fig. 5(b) for 8_4^+ that reveals almost equal contributions of prolate-like and oblate-like configurations). This suggests that the upper sub-band possesses deformed intrinsic states of prolate and oblate deformation, which on average appear near spherical.

The SA basis also provides information about the intrinsic spin. As shown in Ref. [17], the $S = 2$ contribution doubles after the "backbend". Our findings show that the contribution of the $S = 2$ prolate deformations practically remains the same [Fig. 4(c)]. Notably, this increase in the $S = 2$ contribution is a result of the new oblate/triaxial configurations. Overall, there is an equal mixing of prolate and oblate deformations across different S values in the upper sub-band.

2. Intrinsic structure of ^{20}Ne

As discussed above, the *ab initio* SA-NCSM results for ^{20}Ne showed no increase in moment of inertia from $J = 0$ to the "backbend" at $J = 8$ [Fig. 3(b)], which is also supported by the $(\lambda\,\mu)$ and spin decomposition as shown in Fig. 6(a). Indeed, the lowest five states belong to a single rotational band and are all prolate. The dominant deformation for this rotational band is (8 0) $S = 0$, accounting for 50% to 60% of the wave function, as has been found in previous studies (e.g., see [18,61,62]).

Without a change in nuclear structure and microscopic moment of inertia, what produces the apparent anomaly in energies seen in Fig. 1 for ^{20}Ne? Previous studies of Ne isotopes have pointed to rotational alignment as the particles in the *sd* shell align their angular momenta along the rotational axis at the backbend, resulting in an oblate nucleus rotating around its symmetry axis [4,63,64]. This mechanism is identical to that commonly used to explain backbending in heavy nuclei [1]. However, this conflicts with the *ab initio* ^{20}Ne wave functions that reveal highly prolate deformation across $J = 0$–8. With no change in intrinsic structure or angular momentum, the cause of the energy shift at the "backbend" in ^{20}Ne cannot be found looking at the yrast band in isolation as in ^{48}Cr.

Here, the SA-SM results provide a hint [Fig. 6(b)]. Different from the *ab initio* SA-NCSM, the effective SA-SM does not show a constant (8 0) deformation, but instead displays this deformation diminishing toward the "backbend", while the (6 1) $S = 1$ and (4 2) $S = 2$ configurations increasingly mix. Indeed, the smaller fraction of (8 0) for the 8_1^+ state in ^{20}Ne is in line with being dominated by $(d_{5/2})^4$ in the valence-shell model [65], and therefore not very surprising. Further, at $J = 8$ the (6 1) $S = 1$ deformation slightly dominates over the (8 0) $S = 0$. It is interesting to point out that in the SA-SM, there are only three unique intrinsic deformations in the valence shell for 8_1^+, whereas in the SA-NCSM for 11 shells, there are 116 unique intrinsic deformations. Mixing very similar to the one found with the SA-SM is observed in the no-core shell-model results of Ref. [62] with a different chiral potential, larger $\hbar\Omega$ and smaller model spaces compared to the results presented in Fig. 6(a). We note that our SA-NCSM model space includes all the configurations used in Ref. [62] for ^{20}Ne; in addition, we include many other deformations in higher shells without restricting to the (8 0), (6 1), and (4 2)

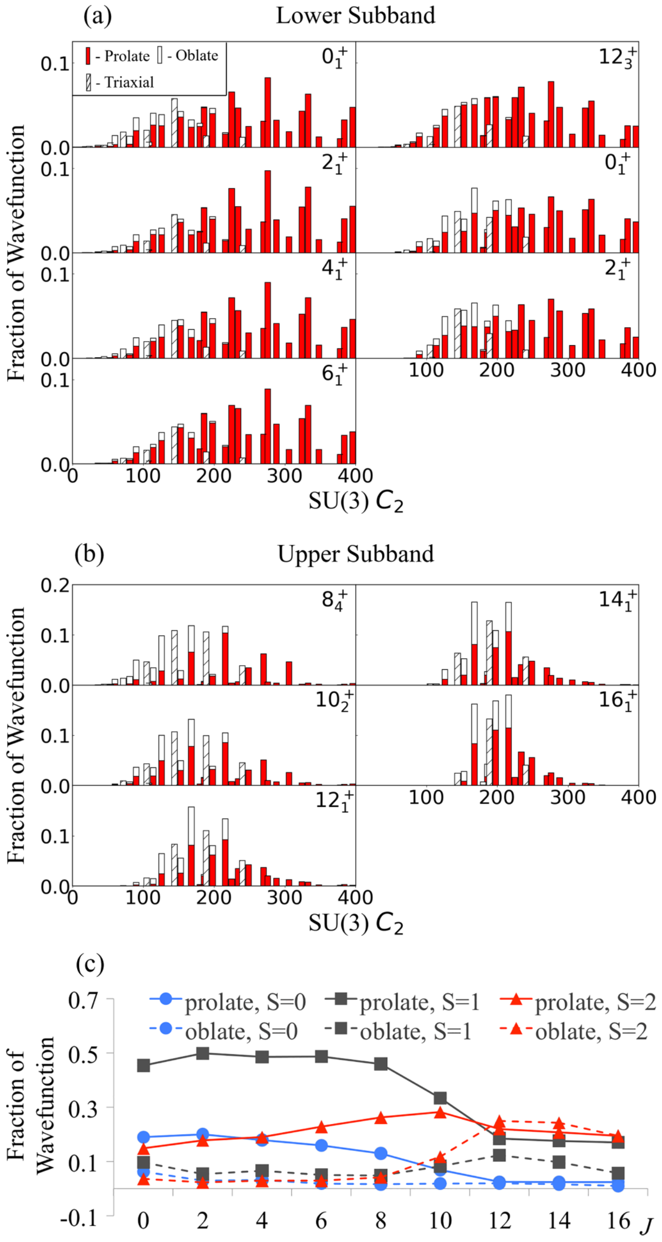

FIG. 4. Decomposition of states in ^{48}Cr with GXPF1 across deformation β (x axis), or equivalently $\mathcal{C}_2 = \frac{3}{2}C_2$ (with the most deformed configurations having the largest C_2) and triaxiality γ (stacked bars: filled red for prolate, unfilled for oblate, and diagonally striped for triaxial deformation). (a) Lower sub-band. (b) Upper sub-band starting at $J = 8$. (c) Spin decomposition of the yrast states (circles for spin zero, squares for spin one, and triangles for spin two) for prolate (solid) and oblate/triaxial (dashed) deformations.

shapes. Indeed, we find that large model spaces are necessary to develop large deformation (equilibrium shapes and their vibrations), such as the highly prolate (8 0) deformation in ^{20}Ne, and to reduce mixing [18]. This is further confirmed by the SA-NCSM results in Fig. 6(a).

The SA-SM large mixing is reminiscent of the lower rotational band of ^{48}Cr which increasingly mixes with the dominant shapes of the upper rotational band around the

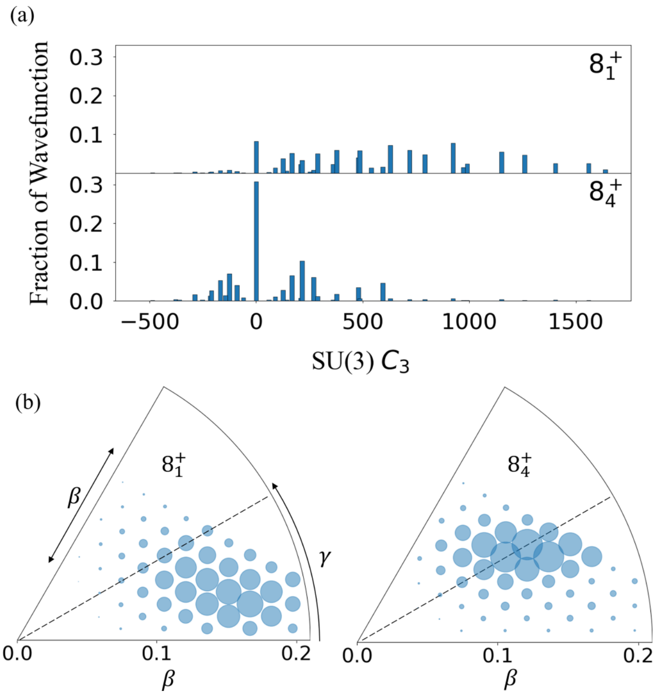

FIG. 5. Comparison of the lower and upper sub-bands of ^{48}Cr at $J = 8$. Wave function decomposition across (a) SU(3) C_3 (with $C_3 > 0$ for prolate, $C_3 = 0$ for triaxial, and $C_3 < 0$ for oblate deformation), and (b) across β and γ, using the domain of $\beta \geqslant 0$ (no effective charges are used). In (b), the area of each circle is proportional to probability and the origin corresponds to the spherical $(\lambda\, \mu) = (0\, 0)$.

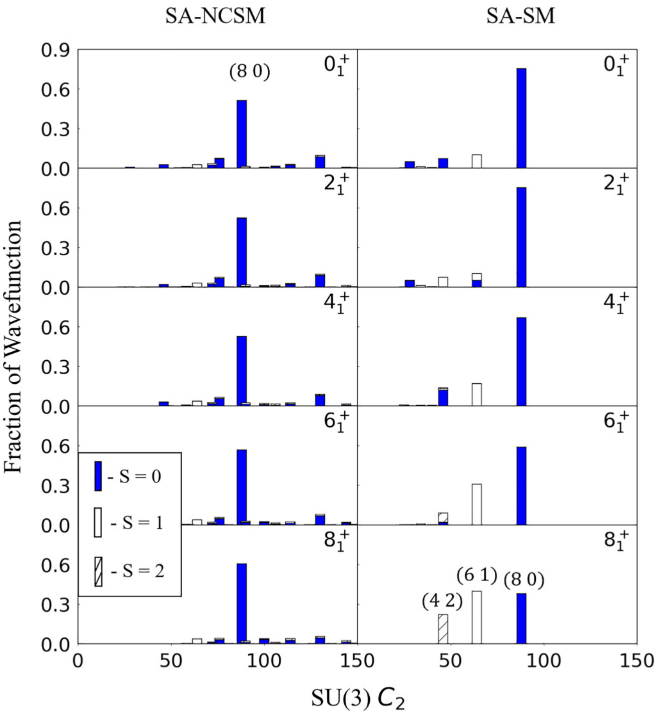

FIG. 6. SU(3) C_2 eigenvalue ($\mathcal{C}_2 = \frac{3}{2}C_2$) and spin decomposition for the yrast band states of ^{20}Ne. (Left) SA-NCSM with the NNLO$_{\text{opt}}$ chiral potential, $N_{\max} = 8$, and $\hbar\Omega = 15$ MeV. (Right) SA-SM with the USDA effective interaction.

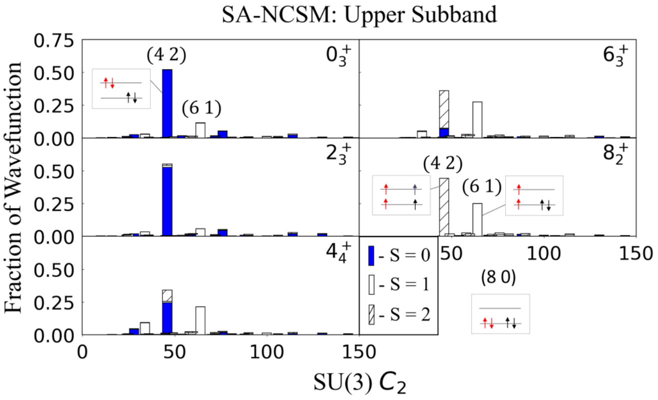

FIG. 7. SU(3) C_2 eigenvalue ($\mathcal{C}_2 = \frac{3}{2}C_2$) and spin decomposition of the upper rotational band states of ^{20}Ne calculated in the SA-NCSM with the NNLO$_{\rm opt}$ chiral potential, $N_{\max} = 8$, and $\hbar\Omega = 15$ MeV. Insets: Spatial distribution of particles within the dominant SU(3) configurations (excluding mirror $p \leftrightarrow n$ configurations). Each level corresponds to specific single-particle excitations in the *sd* shell and can have maximum of four particles [two protons (red) and two neutrons (blue), with spin up (↑) and down (↓)]. For comparison, the most dominant (8 0) of the yrast band is also shown.

"backbend". With this resemblance, we can expect another distinct rotational band lying above the yrast band of ^{20}Ne.

Indeed, in the SA-NCSM framework, we find that the the second excited state of $J = 8$ (8_2^+) is dominated by the two deformations (4 2) $S = 2$ and (6 1) $S = 1$ (Fig. 7), the same deformations we see increasingly mixing in the SA-SM results of Fig. 6. We identify this 8_2^+ state as belonging to a rotational band that extends to $J = 0$ as shown in Fig. 2(b).

From this upper sub-band, we make two primary observations. First, the excited states of this band are either the third or fourth excited state at each value of J. That is, until the "backbend" at $J = 8$, where the 8_2^+ lies directly above the yrast band. Second, approaching the "backbend", we find that (6 1) $S = 1$ and (4 2) $S = 2$ configurations increasingly dominate. (6 1) $S = 1$ is also the most dominant $S = 1$ configuration in the lower sub-band [Fig. 6(a)]. For the dominant intrinsic deformation (4 2), the $S = 2$ configuration starts to dominate over the $S = 0$ configuration at $J = 6$.

These two dominant deformations are the lowest spatial excitations, with (4 2) $S = 2$ representing a proton-proton and neutron-neutron spin-alignment in the *sd* shell, and with (6 1) $S = 1$ representing a proton-proton (or neutron-neutron) spin-alignment (Fig. 7, insets[4]). In other words, we find spin-alignment in the upper rotational band just as it begins to interfere with the yrast band. We also note that (4 2) remains the most dominant configuration throughout the upper sub-band, thereby yielding practically unchanged moment of inertia (spatial degrees of freedom), but its spin structure changes from $S = 0$ at low J to $S = 2$ for high J.

The outcome of this study suggests that for ^{20}Ne, as well as for the heavier ^{48}Cr, spin-aligned configurations at high J interfere with more deformed $S = 0$ configurations. This affects the energy of the states, but with only very little effect on the total moment of inertia and nuclear spatial distribution, in contrast to what the energy spectra in Fig. 2 suggest. This further corroborates the outcome of Ref. [66], where the details of a potential in addition to the rotational energy of a rigid rotor have been found important to reproduce the experimental energies of the ^{166}Er ground state rotational band.

IV. CONCLUSIONS

While energy spectra from both the SA-SM and SA-NCSM replicate the backbending from experimental energies under the rigid-rotor assumption, our microscopic calculations of moment of inertia do not predict a dramatic change in moment of inertia along the yrast bands of ^{20}Ne and ^{48}Cr. Instead, these results suggest that band crossing and spin alignment may significantly affect the energies but only marginally affect intrinsic deformation along the yrast band.

For ^{48}Cr with the GXPF1 effective interaction, we reconcile contradicting predictions of the intrinsic structure after the "backbend". Namely, an almost equal mixing of prolate and oblate intrinsic deformations leads to a nucleus appearing near spherical on average. However, the overall change in deformation from a strongly prolate low-J structure to this mixture of deformed states leads to only a 4% increase in the microscopic moment of inertia.

In ^{20}Ne, the traditional rigid rotor "backbend" is reproduced based on energy levels, however, without any change in intrinsic structure along the yrast band and in the microscopic moment of inertia. We instead find evidence that a spin-aligned upper rotational band mixing with the ground state band leads to a divergence from rigid rotor behavior and has an effect on the excitation energy not on the spatial distribution.

These outcomes do not support rigid shape change as a sole mechanism for the "backbend" of ^{48}Cr as in [8,9,63], while emphasizing the role of band crossing and spin alignment.

Our comparison of the SA-SM and SA-NCSM results in ^{20}Ne points to the need to further explore ^{48}Cr in larger model spaces that are computationally intensive. Primarily, they suggest that the large mixing of deformed states we see in ^{48}Cr with GXPF1 may decrease if the condition of the valence shell is relaxed and excitations to higher shells are included, such as in the SA-NCSM. This is clearly seen in the 8^+ yrast state in ^{20}Ne, where the valence-shell calculations result in a strong mixing in deformation and spin. In contrast, the larger model space in the SA-NCSM allows for the most deformed shape to develop and become dominant. Since *ab initio* SA-NCSM calculations are feasible in the region of ^{48}Cr, future work to study ^{48}Cr from first principles will provide further insight.

---

[4] The single-particle HO basis can be specified by $|n_z n_x n_y\rangle$, the HO quanta in the three Cartesian directions, z, x, and y, with $n_x + n_y + n_z = n$ ($n = 0, 1, 2, \dots$ for s, p, sd,...shells). For a given HO major shell, the complete shell-model space is then specified by all distinguishable distributions of n_z, n_x, and n_y (see, e.g., [18]). For example, for $n = 2$, there are six different distributions, $(n_z, n_x, n_y) = (2, 0, 0)$, $(1, 1, 0)$, $(1, 0, 1)$, $(0, 2, 0)$, $(0, 1, 1)$, and (0,0,2) (the first two configurations are depicted as levels in the insets of Fig. 7).

ACKNOWLEDGMENTS

We thank Marc Verriere for useful discussions. This work was supported in part by the U.S. National Science Foundation (PHY-1913728, PHY-2209060), the Czech Science Foundation (22-14497S), the U.S. Department of Energy, Office of Science, Office of Nuclear Physics, under Grants No. DE-FG02-03ER41272 and No. DE-SC0023532. This work was performed under the auspices of the U.S. Department of Energy by Lawrence Livermore National Laboratory under Contract No. DE-AC52-07NA27344. We thank the National Science Foundation for supporting this work through the REU Site in Physics and Astronomy (NSF Grant No. 1852356) at Louisiana State University. This work benefited from high performance computational resources provided by LSU [67], the National Energy Research Scientific Computing Center (NERSC), a U.S. Department of Energy Office of Science User Facility operated under Contract No. DE-AC02-05CH11231, as well as the Frontera computing project at the Texas Advanced Computing Center, made possible by National Science Foundation Award No. OAC-1818253.

APPENDIX A: TRANSFORMATION TO SU(3)

For completeness, we present the interaction matrix elements used in the SA-SM. In order to introduce a core in the SA-NCSM, we transform the single-particle energies to the SU(3) basis. After expanding the elements in terms of Clebsch-Gordan coefficients, we reduce them to a sum over the orbital and total angular momentum quantum numbers, ℓ and j. For example, one-body SU(3) matrix elements are calculated as

$$\begin{aligned}\varepsilon_{n(\lambda\mu)\kappa(LS)J=0M=0} = {}& (-1)^L\sqrt{2L+1}\sum_{\ell j}(-1)^{1/2+j}\varepsilon_{n\ell j}\\ & \times (2j+1)C^{(\lambda\mu)\kappa L}_{(n0)\ell,(0n)\ell},\\ & \times \begin{Bmatrix}1/2 & \ell & j\\ \ell & 1/2 & L\end{Bmatrix},\end{aligned} \tag{A1}$$

where ε_{nlj} are single-particle energies and $C^{(\lambda\mu)\kappa L}_{(n0)\ell,(0n)\ell}$ are SU(3) reduced Clebsch-Gordan coefficients (with outer multiplicity $\rho = 1$). A similar transformation yields the two-body matrix elements [42].

APPENDIX B: MICROSCOPIC MOMENTS OF INERTIA

For $\lambda \geqslant \mu$, the translationally invariant z component of the moment of inertia $\mathcal{I}_z$ is calculated for a given nuclear state $|J^\pi\rangle$ as

$$\mathcal{I}_z = m\left\langle J\left|\sum_{i=1}^{A}\left(x_i^2+y_i^2\right)\right|J\right\rangle = m\left\langle\sum_{i=1}^{A}\left(r_i^2-z_i^2\right)\right\rangle, \tag{B1}$$

where $\mathbf{r}_i$ is the coordinate of the ith particle relative to the center of mass (for simplicity of notations, we will omit the state parity π and use expectation values $\langle\ldots\rangle$).

The SA-SM and SA-NCSM use laboratory-frame coordinates, and we will first derive $\mathcal{I}_z^{\mathrm{L}}$ for the laboratory frame (L). We will show the steps to remove the center-of-mass contribution in the next section.

In terms of the symplectic Sp(3, $\mathbb{R}$) generators [18] and the oscillator length $b = \sqrt{\frac{\hbar}{m\Omega}}$, the operators needed to calculate $\mathcal{I}_z^{\mathrm{L}}$ are given as

$$\begin{aligned}\frac{1}{b^2}\sum_{i=1}^{A}\left(r_i^{\mathrm{L}}\right)^2 &= \sqrt{\frac{3}{2}}\left(A_0^{(20)}+B_0^{(02)}\right)+H^{(00)}\\ &= \sum_{\alpha=x,y,z}(A_{\alpha\alpha}+B_{\alpha\alpha}+C_{\alpha\alpha}),\end{aligned} \tag{B2a}$$

where $\mathbf{r}_i^{\mathrm{L}}$ is the coordinate of the ith particle in the laboratory frame. The operators A raise a particle two shells up, B are the conjugate lowering operators, and C are the generators of U(3), including the scalar $H^{(00)}$ that counts the total number of HO quanta. In the zth direction, we have

$$\frac{1}{b^2}\sum_i\left(z_i^{\mathrm{L}}\right)^2 = A_{zz}+B_{zz}+C_{zz}. \tag{B3}$$

Therefore,

$$\begin{aligned}\mathcal{I}_z^{\mathrm{L}} &= m\left\langle\sum_i\left[\left(r_i^{\mathrm{L}}\right)^2-\left(z_i^{\mathrm{L}}\right)^2\right]\right\rangle\\ &= mb^2\langle A_{xx}+B_{xx}+C_{xx}+A_{yy}+B_{yy}+C_{yy}\rangle.\end{aligned}$$

Using $C_{zz} = \hat{N}_z$ and $\sum_\alpha C_{\alpha\alpha} = \hat{N}$, where $\hat{N}$ ($\hat{N}_z$) is the operator of the total number of HO quanta (in the z direction), we get

$$\begin{aligned}\mathcal{I}_z^{\mathrm{L}} &= mb^2\langle A_{xx}+A_{yy}+B_{xx}+B_{yy}\rangle + mb^2\langle\hat{N}-\hat{N}_z\rangle\\ &= mb^2\langle\hat{N}-\hat{N}_z\rangle,\end{aligned} \tag{B5}$$

in the laboratory frame. In the last step we use $\langle A_{xx}\rangle = \langle A_{yy}\rangle = \langle B_{xx}\rangle = \langle B_{yy}\rangle = 0$ for valence-shell calculations and $\langle A_{xx}\rangle \simeq 0$, $\langle A_{yy}\rangle \simeq 0$, $\langle B_{xx}\rangle \simeq 0$, $\langle B_{yy}\rangle \simeq 0$ for multishell calculations. These approximations follow from empirical observations; namely, *ab initio* calculations show that excitations are favored first in the z direction, and then in the x direction, making zz and zx the dominant excitations (e.g., see [18]). Almost no excitations occur in the xx or yy directions, allowing us to drop these terms.

APPENDIX C: REMOVAL OF THE CENTER-OF-MASS CONTRIBUTION FOR $\mathcal{I}_z$

Because we use laboratory coordinates in our calculations, we must remove the spurious center-of-mass contribution for $\mathcal{I}_z$. That is, we need to calculate observables using intrinsic coordinates, $\mathbf{r}_i = \mathbf{r}_i^{\mathrm{L}} - \mathbf{R}$, where $\mathbf{R} = \frac{1}{A}\sum_i\mathbf{r}_i^{\mathrm{L}}$ is the center-of-mass coordinate. Therefore, for the z component of the moment of inertia of Eq. (B1), for $\lambda \geqslant \mu$, we calculate

$$\begin{aligned}
&\left\langle \sum_i \mathbf{r}_i{}^2 - \sum_i z_i{}^2 \right\rangle \\
&= \left\langle \sum_i \left(\mathbf{r}_i^{\mathrm{L}} - \mathbf{R}\right)^2 - \sum_i \left(z_i^{\mathrm{L}} - R_z\right)^2 \right\rangle \\
&= \left\langle \sum_i \left(\mathbf{r}_i^{\mathrm{L}}\right)^2 - A\mathbf{R}^2 - \sum_i \left(z_i^{\mathrm{L}}\right)^2 + AR_z^2 \right\rangle \\
&= \left\langle \sum_i \left[\left(\mathbf{r}_i^{\mathrm{L}}\right)^2 - \left(z_i^{\mathrm{L}}\right)^2\right] \right\rangle - A\left\langle \mathbf{R}^2 - R_z^2 \right\rangle. \qquad \text{(C1)}
\end{aligned}$$

The first term is given by Eq. (B5). We now turn to calculating the second term related to the center-of-mass (c.m.).

In the SA-NCSM eigenfunctions, the c.m. is exactly separated from intrinsic degrees of freedom: $|\psi\rangle = |\phi^{\mathrm{CM}}_{N=0,L=0,M=0}\rangle\,|\psi_{int}\rangle$, where

$$\phi^{\mathrm{c.m.}}_{000}(\mathbf{R}) = \langle \mathbf{R}\,|\phi^{\mathrm{c.m.}}_{000}\rangle = \frac{e^{-R^2/2b^2_{\mathrm{c.m.}}}}{\pi^{1/4} b^{3/2}_{\mathrm{c.m.}}} Y_{00}(\hat{R}) \qquad \text{(C2)}$$

is the lowest HO center-of-mass wave function, and $b_{\mathrm{c.m.}} = b/\sqrt{A}$. The c.m. operators in the second term of Eq. (C1) only act on this c.m. wave function, so it suffices to calculate $\int |\phi^{\mathrm{c.m.}}_{000}(R)|^2 R^4 dR$ and $\int |\phi^{\mathrm{c.m.}}_{000}(R)|^2 R_z^2 R^2 dR$, which yield $3b^2/2A$ and $b^2/2A$, respectively. Then,

$$\begin{aligned}
\left\langle \sum_i \left(\mathbf{r}_i{}^2 - z_i{}^2\right) \right\rangle &= b^2\langle \hat{N} - \hat{N}_z\rangle - \frac{3b^2}{2} + \frac{b^2}{2} \\
&= b^2\langle \hat{N} - \hat{N}_z - 1\rangle, \qquad \text{(C3)}
\end{aligned}$$

and $\mathcal{I}_z$ is corrected by only a constant

$$\mathcal{I}_z = mb^2\langle \hat{N} - \hat{N}_z - 1\rangle. \qquad \text{(C4)}$$

Remarkably, $\mathcal{I}_z$ is diagonal in the SU(3) basis with $\hat{N}\,|N(\lambda\,\mu)\rangle = N\,|N(\lambda\,\mu)\rangle$ and $\hat{N}_z\,|N(\lambda\,\mu)\rangle = N_z\,|N(\lambda\,\mu)\rangle$ with $N_z = \frac{1}{3}(2\lambda + \mu + N)$. Hence, the translationally invariant $\mathcal{I}_z$ can be straightforwardly calculated for nuclear wave functions $|J^\pi\rangle$ in the SU(3) basis (3) with probability amplitudes $(c^J_{N(\lambda\,\mu)})^2$,

$$\mathcal{I}_z = mb^2 \sum_{N(\lambda\,\mu)} \left(c^J_{N(\lambda\,\mu)}\right)^2 (N - N_z - 1), \qquad \text{(C5)}$$

and in general, for the $\lambda \geqslant \mu$ and $\lambda < \mu$ cases

$$\begin{aligned}
\frac{2\mathcal{I}_3}{\hbar^2} &= \frac{4}{3\hbar\Omega} \sum_{N(\lambda\,\mu)} \left(c^J_{N(\lambda\,\mu)}\right)^2 \left(N - \frac{3}{2} - \frac{\epsilon}{2}\right), \\
\frac{2\mathcal{I}_1}{\hbar^2} &= \frac{4}{3\hbar\Omega} \sum_{N(\lambda\,\mu)} \left(c^J_{N(\lambda\,\mu)}\right)^2 \left(N - \frac{3}{2} + \frac{\epsilon}{4} - \frac{3}{2}M_\Lambda\right), \\
\frac{2\mathcal{I}_2}{\hbar^2} &= \frac{4}{3\hbar\Omega} \sum_{N(\lambda\,\mu)} \left(c^J_{N(\lambda\,\mu)}\right)^2 \left(N - \frac{3}{2} + \frac{\epsilon}{4} + \frac{3}{2}M_\Lambda\right), \qquad \text{(C6)}
\end{aligned}$$

where ϵ and M_Λ are defined through λ and μ in Eq. (7).

---

[1] F. S. Stephens, Rev. Mod. Phys. **47**, 43 (1975).
[2] A. Faessler, K. R. S. Devi, F. Grümmer, K. W. Schmid, and R. R. Hilton, Nucl. Phys. A **256**, 106 (1976).
[3] P. Ring and P. Schuck, *The Nuclear Many-Body Problem* (Springer, Berlin, Heidelberg, 1980).
[4] K.-H. Speidel, G. J. Kumbartzki, W. Knauer, V. Mertens, P. N. Tandon, N. Ayres de Campos, J. Gerber, and M. B. Goldberg, Phys. Lett. B **92**, 289 (1980).
[5] T. Dytrych, K. D. Launey, J. P. Draayer, D. J. Rowe, J. L. Wood, G. Rosensteel, C. Bahri, D. Langr, and R. B. Baker, Phys. Rev. Lett. **124**, 042501 (2020).
[6] K. D. Launey, A. Mercenne, and T. Dytrych, Annu. Rev. Nucl. Part. Sci. **71**, 253 (2021).
[7] V. Velázquez, J. G. Hirsch, and Y. Sun, Nucl. Phys. A **686**, 129 (2001).
[8] E. Caurier, J. L. Egido, G. Martiñez-Pinedo, A. Poves, J. Retamosa, L. M. Robledo, and A. P. Zuker, Phys. Rev. Lett. **75**, 2466 (1995).
[9] T. Tanaka, K. Iwasawa, and F. Sakata, Phys. Rev. C **58**, 2765 (1998).
[10] G. Martínez-Pinedo, A. Poves, L. M. Robledo, E. Caurier, F. Nowacki, J. Retamosa, and A. Zuker, Phys. Rev. C **54**, R2150 (1996).
[11] A. Juodagalvis, I. Ragnarsson, and S. Aberg, Phys. Lett. B **477**, 66 (2000).
[12] A. Juodagalvis, I. Ragnarsson, and S. Åberg, Phys. Rev. C **73**, 044327 (2006).
[13] P. Roy and S. K. Dhiman, Int. J. Mod. Phys. E **19**, 2265 (2010).
[14] Z. C. Gao, M. Horoi, Y. S. Chen, Y. J. Chen, and Tuya, Phys. Rev. C **83**, 057303 (2011).
[15] K. Hara, Y. Sun, and T. Mizusaki, Phys. Rev. Lett. **83**, 1922 (1999).
[16] J. Ljungberg, B. G. Carlsson, J. Rotureau, A. Idini, and I. Ragnarsson, Phys. Rev. C **106**, 014314 (2022).
[17] R. A. Herrera and C. W. Johnson, Phys. Rev. C **95**, 024303 (2017).
[18] K. D. Launey, T. Dytrych, and J. P. Draayer, Prog. Part. Nucl. Phys. **89**, 101 (2016).
[19] C. Bahri and D. J. Rowe, Nucl. Phys. A **662**, 125 (2000).
[20] T. Dytrych, K. D. Sviratcheva, C. Bahri, J. P. Draayer, and J. P. Vary, Phys. Rev. C **76**, 014315 (2007).
[21] C. W. Johnson, Phys. Rev. C **91**, 034313 (2015).
[22] C. W. Johnson, *Emergent Phenomena in Atomic Nuclei from Large-Scale Modeling: A Symmetry-Guided Perspective* (World Scientific Publishing Co., Singapore, 2017), p. 29.
[23] C. W. Johnson, Phys. Rev. Lett. **124**, 172502 (2020).
[24] D. J. Rowe and J. L. Wood, *Fundamentals of Nuclear Models: Foundational Models* (World Scientific, Singapore, 2010).
[25] S. U. El-Kameesy, H. H. Alharbi, and H. A. Alhendi, AIP Conf. Proc. **831**, 448 (2006).

[26] T. Dytrych, K. D. Sviratcheva, C. Bahri, J. P. Draayer, and J. P. Vary, Phys. Rev. Lett. **98**, 162503 (2007).
[27] P. Ruotsalainen, J. Henderson, G. Hackman, G. H. Sargsyan, K. D. Launey, A. Saxena, P. C. Srivastava, S. R. Stroberg, T. Grahn, J. Pakarinen, G. C. Ball, R. Julin, P. T. Greenlees, J. Smallcombe, C. Andreoiu, N. Bernier, M. Bowry, M. Buckner, R. Caballero-Folch, A. Chester, S. Cruz, L. J. Evitts, R. Frederick, A. B. Garnsworthy, M. Holl, A. Kurkjian, D. Kisliuk, K. G. Leach, E. McGee, J. Measures, D. Mucher, J. Park, F. Sarazin, J. K. Smith, D. Southall, K. Starosta, C. E. Svensson, K. Whitmore, M. Williams, and C. Y. Wu, Phys. Rev. C **99**, 051301(R) (2019).
[28] J. Henderson *et al.*, Phys. Lett. B **782**, 468 (2018).
[29] J. Williams *et al.*, Phys. Rev. C **100**, 014322 (2019).
[30] J. P. Elliott and J. D. Cockcroft, Proc. R. Soc. London A **245**, 128 (1958).
[31] B. J. Verhaar, Nucl. Phys. **21**, 508 (1960).
[32] M. Harvey, Adv. Nucl. Phys. **1**, 67 (1968).
[33] D. J. Millener, J. Math. Phys. **19**, 1513 (1978).
[34] K. T. Hecht and W. Zahn, Nucl. Phys. A **318**, 1 (1979).
[35] D. E. Alburger, C. J. Lister, J. W. Olness, and D. J. Millener, Phys. Rev. C **23**, 2217 (1981).
[36] K. T. Hecht and Y. Suzuki, J. Math. Phys. **24**, 785 (1983).
[37] A. C. Hayes, in *Group Theory and Special Symmetries in Nuclear Physics: Proceedings of the International Symposium in Honor of K.T. Hecht*, edited by J. P. Draayer and J. Jänecke (World Scientific, Singapore, 1992), p. 199.
[38] T. Beuschel, J. P. Draayer, D. Rompf, and J. G. Hirsch, Phys. Rev. C **57**, 1233 (1998).
[39] C. Vargas, J. Hirsch, and J. Draayer, Nucl. Phys. A **690**, 409 (2001).
[40] C. Bahri, D. J. Rowe, and J. P. Draayer, Comput. Phys. Commun. **159**, 121 (2004).
[41] V. K. B. Kota, *SU(3) Symmetry in Atomic Nuclei* (Springer, Singapore, 2020).
[42] K. D. Launey, T. Dytrych, J. P. Draayer, G.-H. Sun, and S.-H. Dong, Int. J. Mod. Phys. E **24**, 1530005 (2015).
[43] G. Rosensteel, Nucl. Phys. A **341**, 397 (1980).
[44] J. Carvalho, R. L. Blanc, M. G. Vassanji, D. J. Rowe, and J. B. McGrory, Nucl. Phys. A **452**, 240 (1986).
[45] J. Carvalho and D. J. Rowe, Nucl. Phys. A **548**, 1 (1992).
[46] J. P. Draayer and Y. Akiyama, J. Math. Phys. **14**, 1904 (1973).
[47] Y. Akiyama and J. P. Draayer, Comput. Phys. Commun. **5**, 405 (1973).
[48] D. J. Rowe, M. G. Vassanji, and J. Carvalho, Nucl. Phys. A **504**, 76 (1989).
[49] D. J. Rowe, Rep. Prog. Phys. **48**, 1419 (1985).
[50] M. T. Mustonen, C. N. Gilbreth, Y. Alhassid, and G. F. Bertsch, Phys. Rev. C **98**, 034317 (2018).
[51] G. Rosensteel and D. J. Rowe, Phys. Rev. Lett. **38**, 10 (1977).
[52] G. K. Tobin, M. C. Ferriss, K. D. Launey, T. Dytrych, J. P. Draayer, A. C. Dreyfuss, and C. Bahri, Phys. Rev. C **89**, 034312 (2014).
[53] Y. Leschber and J. P. Draayer, Phys. Lett. B **190**, 1 (1987).
[54] O. Castaños, J. P. Draayer, and Y. Leschber, Z. Phys. A **329**, 33 (1988).
[55] M. Honma, T. Otsuka, B. A. Brown, and T. Mizusaki, Phys. Rev. C **69**, 034335 (2004).
[56] W. A. Richter, S. Mkhize, and B. A. Brown, Phys. Rev. C **78**, 064302 (2008).
[57] A. Ekström, G. Baardsen, C. Forssén, G. Hagen, M. Hjorth-Jensen, G. R. Jansen, R. Machleidt, W. Nazarewicz *et al.*, Phys. Rev. Lett. **110**, 192502 (2013).
[58] D. J. Rowe, *Emergent Phenomena in Atomic Nuclei from Large-Scale Modeling: A Symmetry-Guided Perspective* (World Scientific Publishing Co., Singapore, 2017), p. 65.
[59] A. Poves, F. Nowacki, and Y. Alhassid, Phys. Rev. C **101**, 054307 (2020).
[60] J. Henderson, Phys. Rev. C **102**, 054306 (2020).
[61] H. Kazama, Prog. Theor. Phys. **77**, 1178 (1987).
[62] R. Zbikowski, C. W. Johnson, A. E. McCoy, M. A. Caprio, and P. J. Fasano, J. Phys. G **48**, 075102 (2021).
[63] E. M. Szanto, A. Szanto de Toledo, H. V. Klapdor, M. Diebel, J. Fleckner, and U. Mosel, Phys. Rev. Lett. **42**, 622 (1979).
[64] K.-H. Speidel, V. Mertens, M. Knopp, W. Trölenberg, H. Neuburger, J. Gerber, and K. Bharuth-Ram, Hyperfine Interact. **15**, 55 (1983).
[65] D. J. Millener, *Invited talk presented to Summer Seminar in Nuclear Theory* (Kingston, Canada, 1976).
[66] D. J. Rowe, Phys. Rev. C **101**, 054301 (2020).
[67] www.hpc.lsu.edu.